# Magnetic porous Fe–C materials prepared by one-step pyrolyzation of NaFe(III)EDTA for adsorptive removal of sulfamethoxazole

Jiandong Zhu[a,†], Liang Wang[a,†], Yawei Shi[a,]*, Bofeng Zhang[b], Yajie Tian[c], Zhaohui Zhang[a], Bin Zhao[a], Guozhu Liu[b,]*, Hongwei Zhang[a,d]

[a]State Key Laboratory of Separation Membranes and Membrane Processes, School of Environmental Science and Engineering, Tiangong University, Tianjin 300387, China, Tel./Fax: +86 22 83955392; emails: shiyawei@tiangong.edu.cn (Y.W. Shi), 1225209391@qq.com (J.D. Zhu), mashi7822@163.com (L. Wang), zzh7448@126.com (Z.H. Zhang), zhaobin@tjpu.edu.cn (B. Zhao), hwzhang@tju.ed (H.W. Zhang)
[b]School of Chemical Engineering and Technology, Tianjin University, Tianjin 300072, China, Tel. +86 22 27892340; emails: gliu@tju.edu.cn (G.Z. Liu), zhangbofeng@tju.edu.cn (B.F. Zhang)
[c]Henan Engineering Research Center of Resource & Energy Recovery from Waste, College of Chemistry and Chemical Engineering, Henan University, Kaifeng 475004, China, email: yjtian@henu.edu.cn (Y.J. Tian)
[d]School of Environmental Science and Engineering, Tianjin University, Tianjin 300072, China

## ABSTRACT

A series of magnetic porous Fe–C materials were prepared by one-step pyrolyzation of ethylene-diaminetetraacetic acid sodium iron(III) at 500°C–800°C and then employed as adsorbents for sulfamethoxazole (SMX) adsorption. The one prepared at 700°C (Fe–C-700) was selected as the optimum one with an adsorption amount of 82.3 mg g$^{-1}$ at pH 5.0 and 30°C. This was mainly ascribed to its higher surface area which offered more space for hydrophobic and electron donor–acceptor interactions between SMX and its surface. The adsorption kinetics was analyzed with three models. With the increase of concentration, the $k_1$ value decreased from 0.383 to 0.329 min$^{-1}$, and the $k_2$ value decreased from 0.0292 to 0.0101 g mg$^{-1}$ min$^{-1}$. The thermodynamic analysis showed that SMX adsorption on Fe–C-700 was a spontaneous exothermic entropy-decreasing process. The effects of adsorbent dosage, pH, metal ions and humic acid on SMX adsorption were also investigated. The spent Fe–C-700 could be easily separated and recycled after adsorption due to its magnetic feature.

*Keywords:* Adsorption; Sulfamethoxazole; Magnetic carbon; Pyrolyzation

## 1. Introduction

Sulfonamide antibiotics are extensively employed for human and animal treatment [1,2]. However, they cannot be metabolized completely and thus can enter the sewage, threatening human health and the environment [3]. Recently, sulfamethoxazole (SMX) as a typical sulfonamide has been frequently detected in the water environment worldwide [4,5]. Among various remediation technologies, the adsorptive method with the merits of easy-operation and absence of additional agents is considered as an efficient approach for its removal [6,7].

Porous carbons with abundant surface areas have long been used as adsorbents, and a variety of porous carbons as efficient adsorbents [8,9] have been prepared from biomass

---

* Corresponding authors.

† These authors contributed equally.

[10–13], metal-organic frameworks (MOFs) [14,15] or organic salts [16]. However, the porous carbons need to be separated from the water after the adsorption process, and the traditional filtration method is inconvenient and time-consuming [17]. Recently, magnetic carbon materials are attracting increasing attention [18]. These materials are composed of carbon and magnetic transition metals/metal compounds, which can be separated rapidly from the aqueous phase by magnetic separation. The magnetic carbon materials can be obtained by a post-treatment method, where a commercial or as-synthesized carbon is impregnated with a metal salt solution and then further treated by hydrothermal heating, pyrolyzation or other methods [19–22]. Another way is the *in-situ* method, where a single precursor is pyrolyzed directly to obtain carbon-metal composite materials. This approach is facile and convenient, but the precursor should be carefully selected. On one hand, the precursor should contain both carbon and metal (Fe, Co, Ni, etc.). On the other hand, considering that porosity is essential for the adsorption process, the precursor should also possess some porosity so that the resulting composite material can inherit the porous structure to some extent. Fe or Co-based MOFs can adequately meet these requirements and have been widely used as precursors [23–26]. However, the preparation procedures of MOFs are relatively complicated, and the commercial products of them are of high prices.

Similar to the MOFs, some organic salts also contain metal cations and organic anions, which can act as iron and carbon sources respectively [27,28]. However, different from MOFs which have well-developed porous structures, these salts are poor in porosity, leading to limited surface areas in the resulting composite materials. For example, the surface area of a Fe–C composite material obtained by pyrolyzation of ferrous gluconate was found to be 34 $m^2$ $g^{-1}$ [28]. Although the surface area was enhanced to 268 $m^2$ $g^{-1}$ after the metal species were removed by acid washing [28], the resulting product was a pure carbon without magnetic property. On the other hand, alkali metal salts have been utilized as precursors to fabricate porous carbons by direct pyrolyzation [29–31]. During the pyrolyzation process, alkali carbonate can be formed *in-situ* and thus promote the formation of pores through carbon activation [29–31].

Inspired by these previous works, an organic salt ethylenediaminetetraacetic acid sodium iron(III) salt (NaFe(III)EDTA) has been employed as the precursor in this work. NaFe(III)EDTA is non-toxic, cheap and commercially available, which is generally used as a food additive for iron fortification [32]. The iron cation and ethylenediaminetetraacetic acid (EDTA) anion in this salt can act as iron and carbon source, while sodium cation can promote the *in-situ* activation process. Due to the unique nature of this salt, porous magnetic carbon can be directly obtained by one-step calcination, which is different from the products obtained with other precursors in previous works. By pyrolyzation of NaFe(III)EDTA at 500°C–800°C, a series of magnetic porous Fe–C composite materials were prepared and then used as adsorbents for the adsorptive removal of SMX from water. The one prepared at 700°C (Fe–C-700) was selected as the optimum one, which was mainly attributed to its higher surface area (169 $m^2$ $g^{-1}$) which offered more space for hydrophobic and electron donor–acceptor (EDA)

interactions between SMX and its surface. The effects of adsorption time, adsorption temperature, adsorbent dosage, pH, metal ions and humic acid on SMX adsorption with Fe–C-700 were investigated in detail. The spent Fe–C-700 could be easily separated after adsorption due to its magnetic feature. The recyclability of Fe–C-700 was also investigated.

## 2. Experimental setup

### 2.1. Materials

NaFe(III)EDTA, AR was obtained from Rhawn Reagent Company (Shanghai, China). SMX, humic acid, ethanol, methanol, acetic acid, NaCl, KCl, CaCl$_2$, NaOH and HCl were all commercially available and details for the manufacturers have been reported previously [16,33]. All the reagents were used as received.

### 2.2. Preparation

~5 g of NaFe(III)EDTA was calcined in flowing nitrogen (30 mL min$^{-1}$) at 500°C–800°C (ramp of 5°C min$^{-1}$) in a furnace tube (Zhonghuan SKG08125K, Tianjin, China). The product was washed with water to neutral pH, dried at 60°C in a vacuum oven for use. The resulting Fe–C materials were marked as Fe–C-500-800 based on the calcination temperature.

### 2.3. Characterization

The Fe–C materials were characterized by scanning electron microscopy (SEM), X-ray diffraction (XRD), CHN elemental analysis, X-ray photoelectron spectroscopy (XPS), Raman, and nitrogen sorption. Detailed information can be found in our previous works [16,33]. The magnetic property was investigated with a superconducting quantum interference device (SQUID, Quantum Design MPMS XL-7, USA).

### 2.4. Adsorption experiments

Aqueous SMX solutions were prepared with no co-solvent and then adjusting the pH to 5.0 ± 0.1. A certain amount of Fe–C material and SMX solution were added into a glass flask, and the mixture was stirred by mechanical stirring at 200 rpm at 30°C in a water bath. Samples were withdrawn with syringe filters (PTFE, 0.22 μm). Kinetic and isothermal studies were conducted by adding 50 mg Fe–C-700 to 100 mL solution at initial SMX concentration ($C_0$) of 25–100 mg L$^{-1}$. SMX concentration was measured by high-performance liquid chromatography (HPLC, LC-20AT, Shimadzu, Japan) [33]. The adsorption of SMX was also conducted at 20°C and 40°C to study the temperature effect. 100 mM NaCl, KCl or CaCl$_2$ was added when needed at $C_0$ = 50 mg L$^{-1}$. 10–100 mg L$^{-1}$ humic acid was added when needed. The adsorbent (0.5 g L$^{-1}$) after adsorption at $C_0$ = 50 mg L$^{-1}$ was separated and extracted with ethanol (100 mL per 50 mg fresh Fe–C-700) for the next adsorption run. In this work, the adsorption experiments were performed for at least twice according to previous works [21,34].

## 3. Results and discussion

### 3.1. Characterizations of the Fe–C materials

As observed in the SEM images (Figs. 1a and b), the morphology of Fe–C-700 possessed aggregates of spherical particles embedded in a rough matrix. XRD patterns (Fig. 1c) revealed the phase compositions of the Fe–C materials. The weak peak around 25° was attributed to amorphous carbon, while other peaks were indexed to Fe-containing materials [35]. Considering the tiny difference between the standard patterns of $Fe_3O_4$ (JCPDS 19–0629) and $\gamma$-$Fe_2O_3$ (JCPDS 39–1346), the peaks marked with a diamond symbol were attributed to both phases. The peak intensity of iron oxides declined with increasing pyrolyzation temperature. Diffraction peaks of $Fe_3C$ (JCPDS 35-0772) and Fe (JCPDS 06-0696) emerged on the patterns of Fe–C-600 and Fe–C-700, indicating the reduction of iron oxide by carbon [36]. For Fe–C-800, Fe became the major phase, which was ascribed to the decomposition of $Fe_3C$ ($Fe_3C \rightarrow 3Fe + C$) at higher temperature [37]. Raman spectra (Fig. 1d) show the D and G bands of carbon, indicating the amorphous nature of carbon in the materials. XPS measurements were further performed to characterize the oxidation states of iron in the Fe–C materials (Fig. 2). The presence of both Fe(II)

and Fe(III) was revealed [38,39], again verifying the reduction of Fe(III) by carbon during the pyrolyzation process. Moreover, Fe(0) was found in the spectra of Fe–C-600, 700 and 800 [38,39], in accordance with XRD results. The peak intensity of Fe(0) was much lower compared to that of Fe(II) or Fe(II), which was attributed to the surface oxidation of Fe(0) during the preparation and storage of the materials [40]. As shown in Fig. 3a, the high-resolution C1s spectrum of Fe–C-700 can be deconvoluted into four components, which were assigned to C–C, C–O, C–N and C=O species. In Fig. 3b, the high-resolution N1s spectrum of Fe–C-700 can be deconvoluted into three components, which were assigned to N–H, –$NH_2$ or –NH and –$CNH_2$. According to previous works [14,20,22,41], these functional groups on the carbon surface may interact with SMX through hydrogen-bonding, favoring the adsorption of the SMX.

The specific surface areas ($S_{BET}$) of the Fe–C materials were summarized in Table 1. An increase in $S_{BET}$ was observed from Fe–C-500 to Fe–C-700. During the pyrolyzation of sodium-containing organic salts, sodium carbonate was generated and then decomposed to form carbon dioxide ($Na_2CO_3 \rightarrow Na_2O + CO_2$) [29], which then paved the classical physical activation process to ($C + CO_2 \rightarrow 2CO$) to introduce pores into the carbon structure [29]. Due to the endothermic
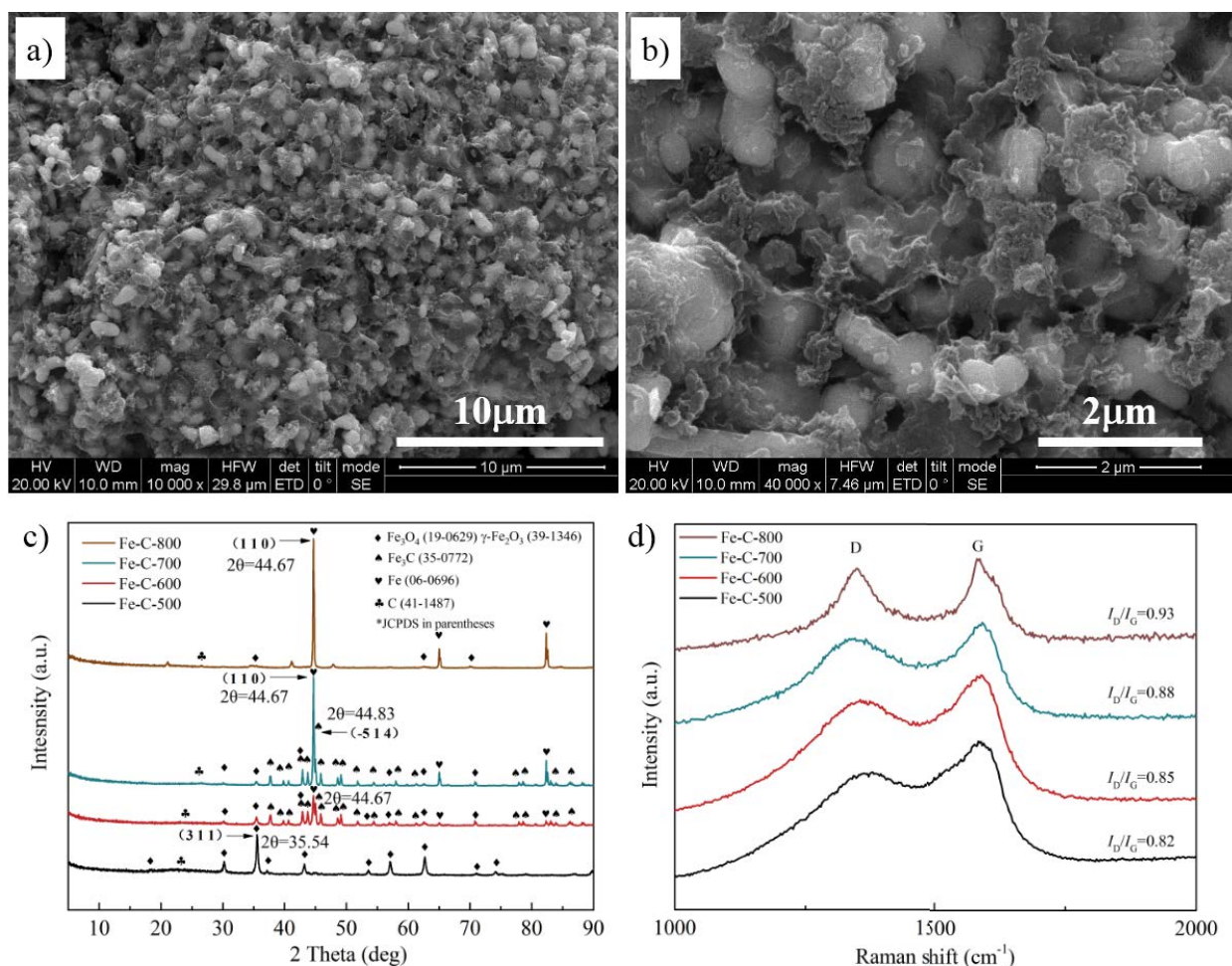


Fig. 1. (a,b) SEM images of Fe–C-700, (c) XRD patterns and (d) Raman spectra of the Fe–C materials.
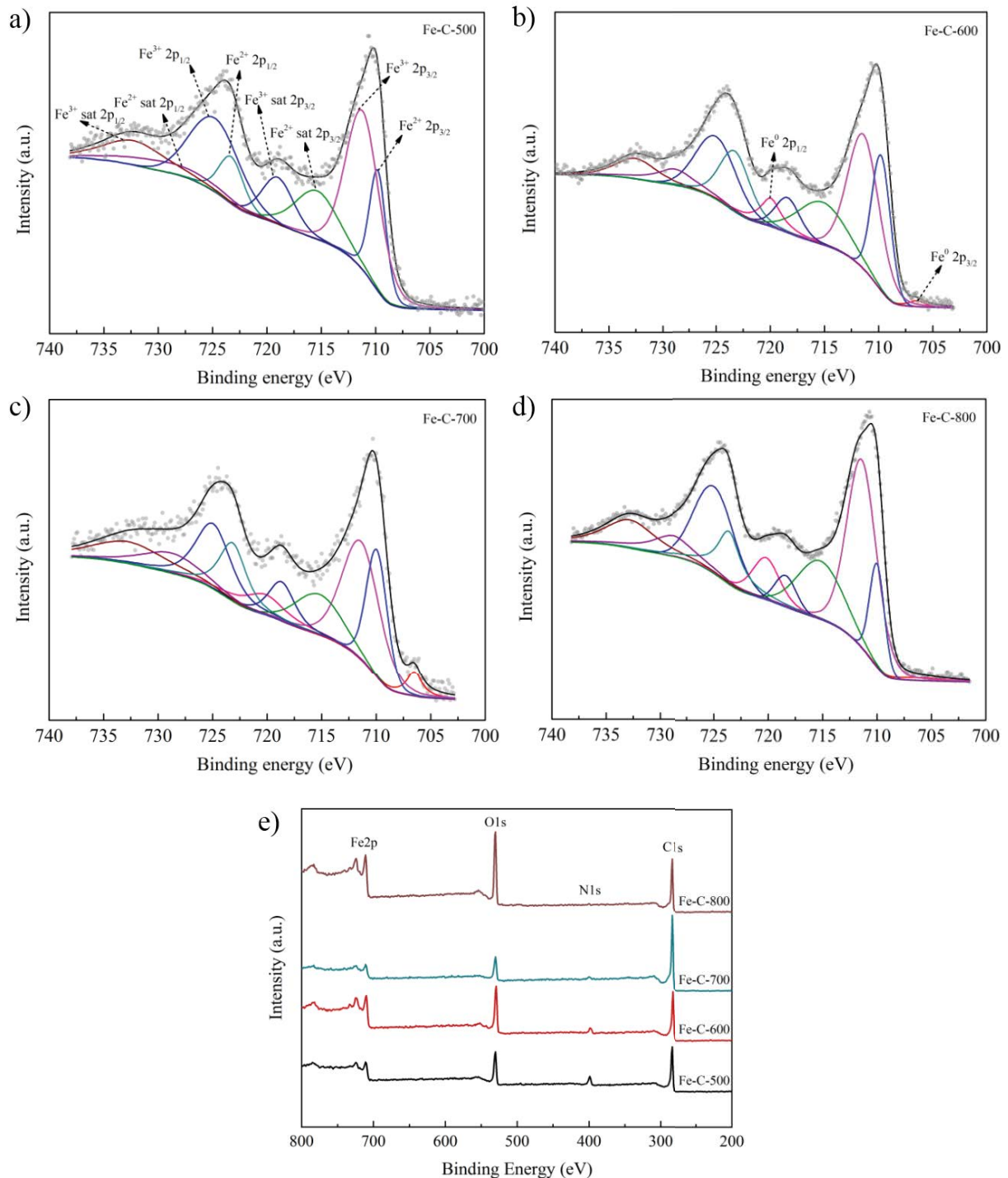
Fig. 2. High-resolution XPS Fe 2p spectra of the Fe–C materials and the survey scan XPS spectra of the Fe–C materials.

nature of the activation reaction [42], a higher pyrolyzation temperature would lead to enhanced etching of the carbon structure and thus better-developed porosity. This was also reflected from the increased $I_D/I_G$ ratios obtained from Raman results (Fig. 1d) with increasing pyrolyzation temperature because more severe etching would introduce more defects into the carbon framework. However, the surface area of

Fe–C-800 dropped dramatically compared to Fe–C-700. The generation of porosity meant the consumption of carbon during the activation process. Carbon was also consumed through the reduction of Fe(III) into Fe(II)/Fe(0) as discussed above. With increasing temperature, more carbon was gasified while iron remained in the resulting materials. As shown in Table 1, the contents of carbon determined by XPS did not
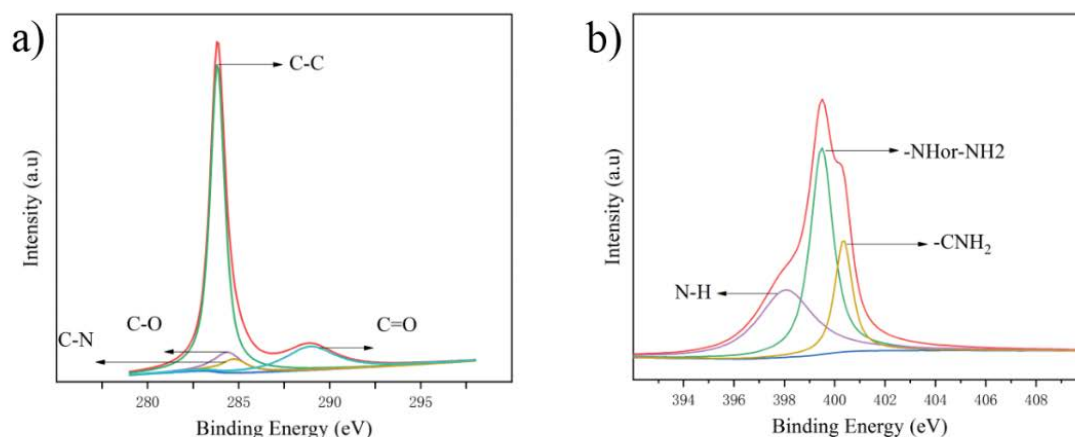
Fig. 3. (a) C1s spectra of Fe–C-700 and (b) N1s spectra of Fe–C-700.

Table 1
Textural properties and elemental compositions of the Fe–C adsorbents

| Sample | $S_{BET}$[a] | $V_{total}$[b] | C[c] | N[c] | Fe[c] | O[c] | C[d] | N[d] | H[d] |
|---|---|---|---|---|---|---|---|---|---|
| Fe–C-500 | 43 | 0.047 | 48.6 | 7.4 | 22.3 | 21.7 | 25.93 | 4.92 | 1.66 |
| Fe–C-600 | 135 | 0.140 | 40.7 | 3.6 | 32.5 | 23.1 | 24.64 | 2.63 | 1.54 |
| Fe–C-700 | 169 | 0.149 | 68.8 | 2.2 | 15.3 | 13.7 | 20.56 | 0.53 | 1.54 |
| Fe–C-800 | 19 | 0.040 | 34.7 | 0.7 | 35.7 | 29.0 | 6.02 | 0.48 | 1.30 |

[a]$m^2 \, g^{-1}$·[b]$cm^3 \, g^{-1}$[c]mass percentage (%) determined by XPS;
[d]mass percentage (%) determined by CHN elemental analysis.

following the expected declining trend because XPS could only tell the surface compositions. CHN elemental analysis which could reveal the bulk compositions were additionally conducted and a declining trend was clearly observed (Table 1). The surface carbon content was larger than the bulk carbon content for all the four samples, indicating the surface enrichment of carbon, which was probably attributed to the partial wrap up of iron species by carbon. The nitrogen element detected in all the samples was inherent from the NaFe(II)EDTA precursor. The decreased content of nitrogen with rising temperature was ascribed to the decomposition of nitrogen-containing functional groups, similar to the case when EDTA-4Na was employed as the precursor [43].

*3.2. Isotherm, thermodynamic and kinetic study*

The Fe–C materials prepared were compared for SMX adsorption. As illustrated in Fig. 4a, the adsorption amount increased with the rising initial concentration of SMX until saturation was reached. The Langmuir model (Eq. (1)) was employed to build the adsorption isotherms by non-linear fitting (Table 2). The maximum adsorption amount ($q_{max}$) increased from Fe–C-500 to Fe–C-700 and then declined for Fe–C-800, in accordance with the trend in $S_{BET}$. The positive linear trend ($R^2 = 0.825$) was further revealed by plotting $q_{max}$ against $S_{BET}$ (Fig. 4b). Based on our previous works [44,45] and the result here, it was inferred that hydrophobic interaction and EDA interaction were the dominant adsorption mechanisms for SMX adsorption. The adsorption experiments were conducted at pH 5.0 where SMX mainly existed as neutral molecules [14,46], thus electrostatic interaction should have played a less important role. A greater surface area offered more space for hydrophobic and EDA interactions between the adsorbent surface and SMX, favoring the adsorption amount of the latter.

$$q_e = \frac{q_{max}K_L C_e}{\left(1 + K_L C_e\right)} \tag{1}$$

Using Fe–C-700 as the optimum adsorbent, the adsorption isotherms at 20°C and 40°C were built furthermore for thermodynamic analysis (Fig. 5). A decline in $q_{max}$ was revealed with increasing adsorption temperature (Table 3). The standard enthalpy and entropy changes were calculated to be –23.29 kJ mol$^{-1}$ and –2.41 J mol$^{-1}$ K$^{-1}$ by fitting in the van't Hoff equation (Eq. (2)). The negative $\Delta H°$ value indicated that the adsorption of SMX on Fe–C-700 was an exothermic process. The negative $\Delta S°$ value was attributed to the loss of freedom caused by the transport of free SMX in aqueous solution to the solid phase. The Gibbs free energy changes ($\Delta G°$) obtained from Eq. (3) were around –22 kJ mol$^{-1}$ (Table 3), which fell in the range of 12–25 kJ mol$^{-1}$ estimated previously for $\pi$–$\pi$ EDA interaction [47,48], suggesting that EDA interaction played an important role.
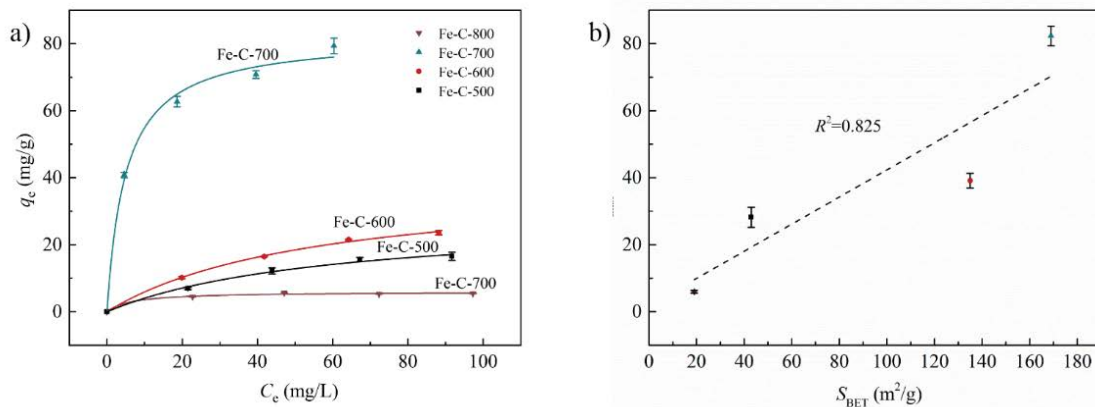
Fig. 4. (a) Langmuir adsorption isotherms for SMX on the Fe–C materials and (b) effect of surface area on the adsorption amount of SMX. ($T$ = 30°C; adsorbent dosage 0.5 g L$^{-1}$; pH = 5).
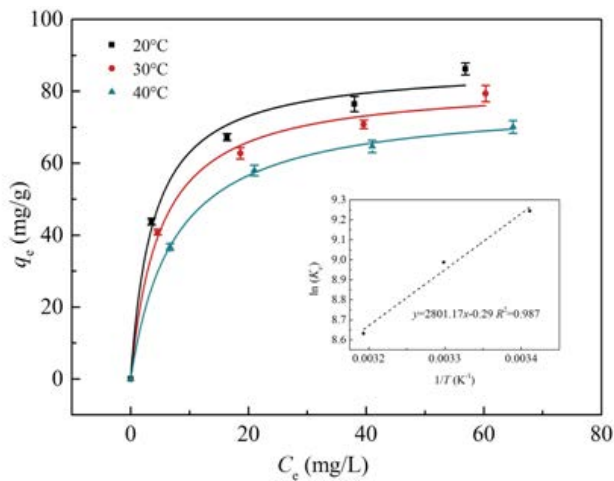


Fig. 5. Adsorption isotherms for SMX on Fe–C-700 at 20°C–40°C and fitting in van't Hoff equation (inset). (pH = 5; adsorbent dosage 0.5 g L$^{-1}$).

$$\ln\left(K_c\right) = \frac{-\Delta H°}{RT} + \frac{\Delta S°}{R} \tag{2}$$

$$\Delta G° = \Delta H° - T\Delta S° \tag{3}$$

Kinetic analysis was conducted with Fe–C-700 at three initial concentrations ($C_0$).

As compared in Fig. 6a and Table 4, the experimental data were better non-linearly fitted in the pseudo-second-order model (Eq. (4)) compared to the pseudo-first-order one (Eq. (5)). Recently it has been demonstrated that fitting in these two kinetic models cannot lead to direct assignment of adsorption mechanisms [49]. Despite this, the increase of initial adsorption rate ($h$) calculated from Eq. (6) along with $C_0$ (Table 4) could be attributed to the stronger diffusion driving force [9]. The intraparticle diffusion model (Eq. (7)) was furthermore employed to analyze the kinetic data. The multi-linear curves (Fig. 6b) were ascribed to the multistep adsorption process including boundary layer

**Table 2**
Langmuir isotherm model for SMX adsorption on the Fe–C adsorbents ($T$ = 30°C; adsorbent dosage 0.5 g L$^{-1}$; pH = 5)

| Sample | Langmuir model | | | |
|---|---|---|---|---|
| | $q_{max}$ (mg g$^{-1}$) | $K_L$ (L mg$^{-1}$) | $R^2$ | $R_L$ |
| Fe–C-500 | 28.2 | 0.0168 | 0.993 | 0.37–0.70 |
| Fe–C-600 | 39.1 | 0.0178 | 0.998 | 0.36–0.69 |
| Fe–C-700 | 82.3 | 0.2005 | 0.992 | 0.05–0.17 |
| Fe–C-800 | 6.0 | 0.1520 | 0.984 | 0.06–0.21 |

diffusion and intraparticle diffusion [50]. The rate constants declined along with the time ($k_1 > k_2$, Table 5), indicating that the adsorbent surface gradually approached saturation [51]. The increased $C_i$ value was attributed to stronger boundary layer diffusion [52].

$$q_t = \frac{q_e^2 k_2 t}{\left(1 + q_e k_2 t\right)} \tag{4}$$

$$q_t = q_e\left(1 - \exp\left(-k_1 t\right)\right) \tag{5}$$

$$h = k_2 q_e^2 \tag{6}$$

$$q_t = k_i t^{0.5} + C \tag{7}$$

### 3.3. Effect of adsorbent dosage, pH, metal ions and humic acid

The adsorption of SMX was performed with different dosages of Fe–C-700 (Fig. 7a). The adsorption amount dropped with increasing adsorbent dosage as expected, which was ascribed to the availability of more abundant adsorption sites [44,53]. The effect of pH on SMX adsorption was conducted at a series of pH values higher than 5.0 because lower pH values would lead to the dissolution of the adsorbent. As illustrated in Fig. 7b, the adsorption of SMX was suppressed with increasing pH values. At higher

Table 3
Adsorption thermodynamics and Langmuir isotherm models for SMX adsorption on Fe–C-700 at 20°C–40°C (adsorbent dosage 0.5 g L$^{-1}$; pH = 5)

| $T$ (°C) | Langmuir model | | | | Adsorption thermodynamics | | |
|---|---|---|---|---|---|---|---|
| | $q_{max}$ (mg g$^{-1}$) | $K_L$ (L mg$^{-1}$) | $R^2$ | $R_L$ | $\Delta G°$ (kJ mol$^{-1}$) | $\Delta H°$ (kJ mol$^{-1}$) | $\Delta S°$ (J mol$^{-1}$ K$^{-1}$) |
| 20 | 87.2 | 0.2605 | 0.988 | 0.04–0.13 | −22.59 | −23.29 | −2.41 |
| 30 | 82.3 | 0.2005 | 0.992 | 0.05–0.17 | −22.56 | | |
| 40 | 77.4 | 0.1361 | 0.999 | 0.07–0.23 | −22.54 | | |

Table 4
Pseudo-first-order and pseudo-second-order models for SMX adsorption on Fe–C-700 (adsorbent dosage 0.5 g L$^{-1}$; $T$ = 30°C; pH = 5)

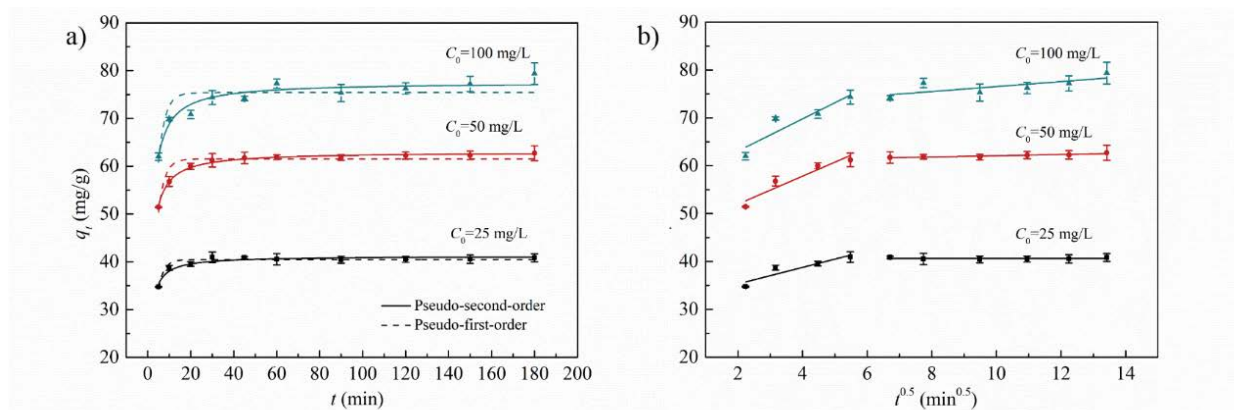| $C_0$ (mg L$^{-1}$) | Pseudo-first-order model | | | Pseudo-second-order model | | | |
|---|---|---|---|---|---|---|---|
| | Cal. $q_e$ (mg g$^{-1}$) | $k_1$ (min$^{-1}$) | $R^2$ | Cal. $q_e$ (mg g$^{-1}$) | $k_2$ (g mg$^{-1}$ min$^{-1}$) | $R^2$ | $h$ (mg g$^{-1}$ min$^{-1}$) |
| 25 | 40.5 | $3.83 \times 10^{-1}$ | 0.916 | 41.2 | $2.92 \times 10^{-2}$ | 0.923 | 49.6 |
| 50 | 61.5 | $3.43 \times 10^{-1}$ | 0.865 | 63.0 | $1.44 \times 10^{-2}$ | 0.993 | 57.2 |
| 100 | 75.4 | $3.29 \times 10^{-1}$ | 0.729 | 77.6 | $1.01 \times 10^{-2}$ | 0.920 | 60.8 |



Fig. 6. (a) Pseudo-first-order and pseudo-second-order models and (b) intraparticle diffusion model for SMX adsorption on Fe–C-700. ($T$ = 30°C; adsorbent dosage 0.5 g L$^{-1}$; pH = 5).

Table 5
Intraparticle diffusion constants for SMX adsorption on Fe–C-700

| $C_0$ (mg L$^{-1}$) | $k_1$ (mg g$^{-1}$ min$^{-0.5}$) | $C_1$ (mg g$^{-1}$) | $R_1^2$ | $k_2$ (mg g$^{-1}$ min$^{-0.5}$) | $C_2$ (mg g$^{-1}$) | $R_2^2$ |
|---|---|---|---|---|---|---|
| 25 | 1.72 | 31.9 | 0.856 | 0 | 40.6 | 0 |
| 50 | 2.92 | 46.2 | 0.913 | 0.13 | 60.8 | 0.849 |
| 100 | 3.36 | 56.4 | 0.849 | 0.52 | 71.4 | 0.565 |

pH values, deprotonation of SMX occurred, weakening hydrophobic and EDA interactions [11,44]. Electrostatic repulsion between deprotonated SMX and the adsorbent surface may also contribute to the decreased adsorption amount. According to zeta potential measurements (Fig. 7c), the surface of Fe–C-700 was negatively charged at pH > 8.47 and positively charged at pH < 8.47. SMX has two pKa values of 1.6 and 5.7 [16]. At 1.6 < pH < 5.7, SMX mainly existed in a neutral form and the effect of electrostatic force was limited. At 5.7 < pH < 8.5, electrostatic attraction existed between SMX$^-$ and the Fe–C-700 surface, and the decreased adsorption amount was partially ascribed to the weakened electrostatic attraction with increasing pH value. At pH > 8.5, increased electrostatic repulsion between deprotonated SMX and the adsorbent surface also contributed to the decreased adsorption amount.

The above adsorption experiments were all conducted in deionized water. Natural water contains abundant

inorganic ions and natural organic matters, and these species may impact the adsorption of SMX. For potential practical applications, effect of typical metal ion ($Na^+$, $K^+$ or $Ca^{2+}$) was first investigated. The metal ions were added as chloride salts, and no pH adjustment was conducted upon their addition. As illustrated in Fig. 7d, the addition of 100 mM $Na^+$ or $K^+$ had no obvious impact on the adsorption amount of SMX, while the addition of 100 mM $Ca^{2+}$ significantly suppressed SMX adsorption. NaCl and KCl as strong acid–strong base salts do not influence the solution pH. As expected, the solution pH remained constant with

the addition of NaCl or KCl. $CaCl_2$ is known as a strong acid–weak base salt and its hydrolysis may impact the solution pH. Surprisingly, it was found that after the dissolution of 100 mM $CaCl_2$ into 50 mg $L^{-1}$ SMX, the pH of the solution rose dramatically from 5.0 to 9.2. This was unexpected because hydrolysis of $Ca^{2+}$ could not generate $OH^-$. It was inferred that a trace amount of $Ca(OH)_2$ impurity existed in the analytic grade regent of $CaCl_2$ due to its production procedure. An extra experiment was conducted by tailoring the pH to 5.0 by HCl after the addition of $CaCl_2$. Under this condition, the significant suppression effect of $Ca^{2+}$ on
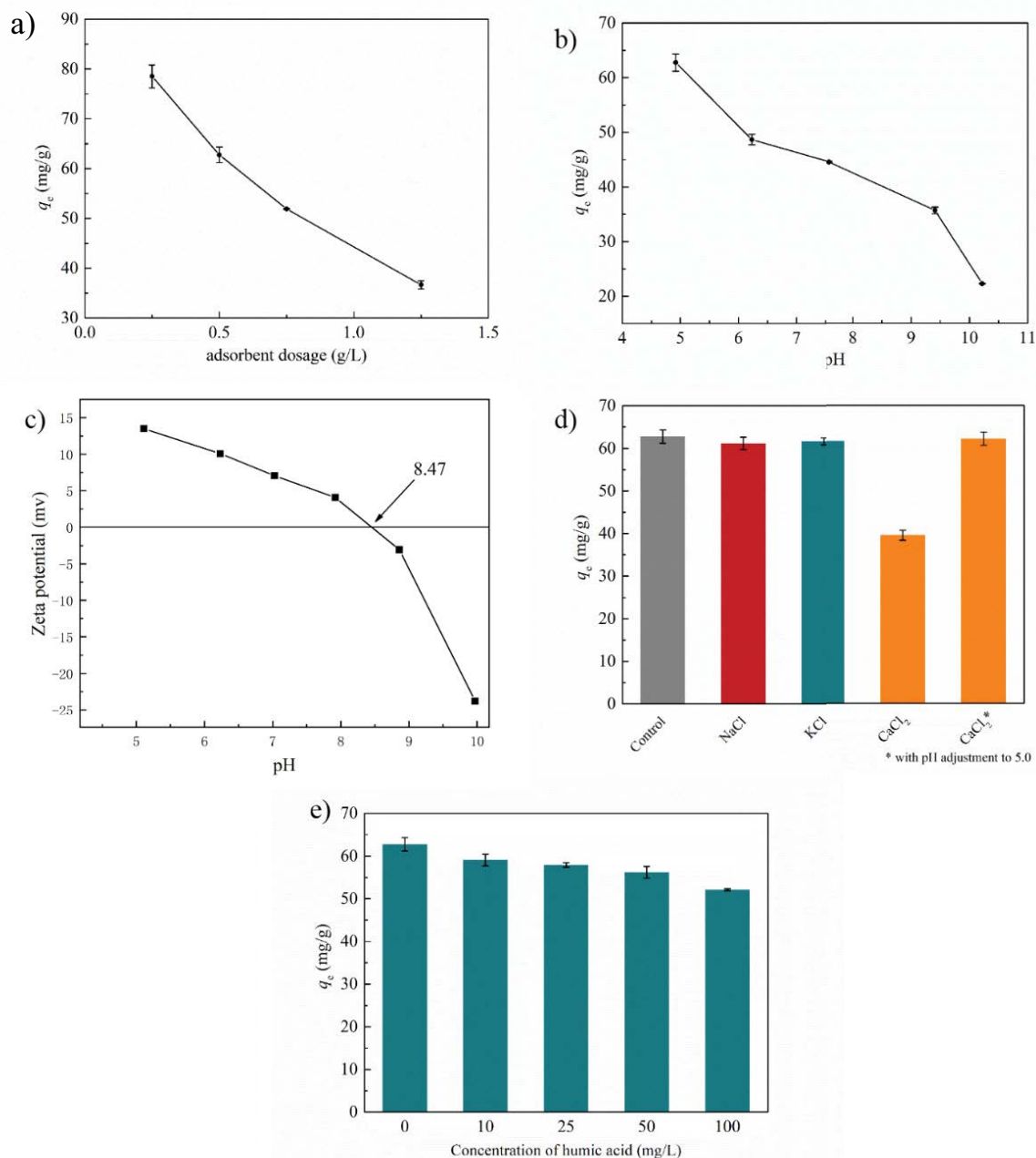


Fig. 7. (a) Effect of adsorbent dosage, (b) pH, (c) the zeta potential of Fe–C-700 at different pH values, (d) effect of metal ions and (e) humic acid. ($T$ = 30°C (a,b,d,e); initial SMX concentration 50 mg $L^{-1}$ (a,b,d,e); adsorbent dosage 0.5 g $L^{-1}$ (b,d,e)).
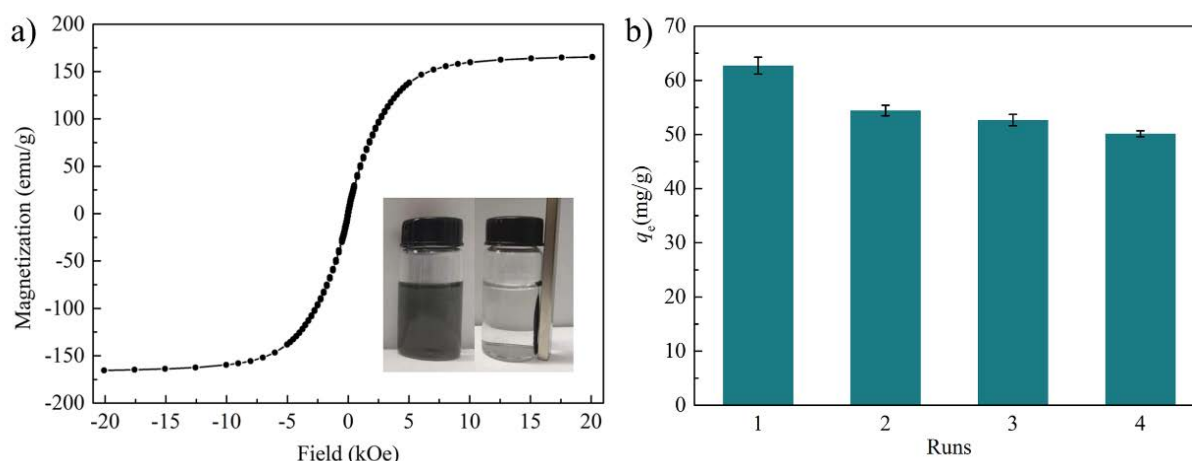
Fig. 8. (a) Magnetization curve of Fe–C-700 (inset: the photo of magnetic separation) and (b) recyclability of Fe–C-700.

SMX adsorption evaporated. The insignificant impact of metal ions on SMX adsorption again indicated that electrostatic interaction was less important at an intermediate pH, in accordance with the discussions in section 3.2 (isotherm, thermodynamic and kinetic study).

The effect of humic acid (HA) on SMX adsorption was further studied. The pH effect was ruled out by adjusting the HA stock solution to pH 5.0. As observed in Fig. 7e, the adsorption amount of SMX decreased with increasing HA concentration. The aromatic structure of HA [54] endowed it the ability to be adsorbed through EDA interaction, occupying the adsorbent surface and acting as a competitor in the adsorption process of SMX [11].

### 3.4. Recyclability and comparison with other adsorbents

The magnetic behavior of Fe–C-700 was displayed in Fig. 8a. The saturation magnetization (Ms) of Fe–C-700 approached 165 emu g$^{-1}$, making it easy to separate the adsorbent with an external magnetic field (Fig. 8a inset). The spent Fe–C-700 was extracted by ethanol and then used for the next adsorption run. Ethanol or methanol was widely used in previous works for the regeneration of carbon materials [12,14]. The adsorption equilibrium is dynamic. Since the solubility of SMX in ethanol is much greater than that in water, the solid–liquid equilibrium distribution coefficient in ethanol should be much smaller than that in water. Besides, the regeneration time was long enough for the desorption of SMX. After four adsorption runs, the adsorption amount of SMX decreased to 50.1 mg g$^{-1}$ (Fig. 8b), which was about 80% of that of the fresh adsorbent. The result indicated the acceptable recyclability of Fe–C-700 for SMX adsorption.

Some previous materials possessed larger SMX adsorption amounts than Fe–C-700. However, the Fe–C-700 in this work possessed a magnetic feature and could be easily separated after adsorption. Besides, it was prepared facilely by a one-step *in-situ* pyrolyzation method, different from the post-treatment method usually employed previously for the fabrication of magnetic carbons. Considering these merits, Fe–C-700 could be considered promising for SMX removal from the water environment.

## 4. Conclusions

A series of magnetic porous Fe–C materials were prepared facilely by direct pyrolyzation of NaFe(III)EDTA at 500°C–800°C. Different from carbon precursors used by predecessors, porous magnetic carbon can be directly obtained by calcination with NaFe(III)EDTA as the precursor, which shows a good adsorption effect and has potential application in water treatment. Nitrogen sorption results verified the porous nature of these materials, and the compositions of them changed with the pyrolyzation temperature as revealed by XRD, XPS and EA measurements. The one prepared at 700°C (Fe–C-700) was selected as the optimum one with a $q_{max}$ of 82.3 mg g$^{-1}$ at pH 5.0 and 30°C. This was mainly ascribed to its higher surface area which offered more space for hydrophobic and EDA interactions between SMX and its surface. With the increase of concentration, $k_1$ value decreased from 0.383 to 0.329 min$^{-1}$, and $k_2$ value decreased from 0.0292 to 0.0101 g mg$^{-1}$ min$^{-1}$. Thermodynamic analysis indicated that SMX adsorption on Fe–C-700 was an entropy-decreasing process. SMX adsorption was suppressed with increasing pH or in the presence of humic acid, while the effects of metal ions including Na$^+$, K$^+$ and Ca$^{2+}$ were limited. The spent Fe–C-700 could be easily separated and recycled after adsorption due to its magnetic feature.

## Acknowledgments

## References

[1] Y.X. Gao, R.X. Kang, J. Xia, G. Yu, S.B. Deng, Understanding the adsorption of sulfonamide antibiotics on MIL-53s: metal dependence of breathing effect and adsorptive performance in aqueous solution, J. Colloid Interface Sci., 535 (2019) 159–168.

[2] S.X. Guo, M.L. Gao, T. Shen, Y. Xiang, G.L. Cao, Effective adsorption of sulfamethoxazole by novel Organo-Vts and their mechanistic insights, Microporous Mesoporous Mater., 286 (2019) 36–44.

[3] W.W. Ben, B. Zhu, X.J. Yuan, Y. Zhang, M. Yang, Z.M. Qiang, Occurrence, removal and risk of organic micropollutants in wastewater treatment plants across China: comparison of wastewater treatment processes, Water Res., 130 (2018) 38–46.

[4] W. Gwenzi, N. Chaukura, Organic contaminants in African aquatic systems: current knowledge, health risks, and future research directions, Sci. Total Environ., 619–620 (2018) 1493–1514.

[5] B. Díaz-Garduño, M.G. Pintado-Herrera, M. Biel-Maeso, J.J. Rueda-Márquez, P.A. Lara-Martín, J.A. Perales, M.A. Manzano, C. Garrido-Pérez, M.L. Martín-Díaz, Environmental risk assessment of effluents as a whole emerging contaminant: efficiency of alternative tertiary treatments for wastewater depuration, Water Res., 119 (2017) 136–149.

[6] M. Zbair, H. Ait Ahsaine, Z. Anfar, Porous carbon by microwave assisted pyrolysis: an effective and low-cost adsorbent for sulfamethoxazole adsorption and optimization using response surface methodology, J. Cleaner Prod., 202 (2018) 571–581.

[7] S.G. Akpe, I. Ahmed, P. Puthiaraj, K.S. Yu, W.-S. Ahn, Microporous organic polymers for efficient removal of sulfamethoxazole from aqueous solutions, Microporous Mesoporous Mater., 296 (2020) 109979.

[8] A.A. Alswat, M.B. Ahmad, T.A. Saleh, Zeolite modified with copper oxide and iron oxide for lead and arsenic adsorption from aqueous solutions, J. Water Supply Res. Technol. AQUA, 65 (2016) 465–479.

[9] T.A. Saleh, Isotherm, kinetic, and thermodynamic studies on Hg(II) adsorption from aqueous solution by silica- multiwall carbon nanotubes, Environ. Sci. Pollut. Res. Int., 22 (2015) 16721–16731.

[10] M.B. Ahmed, J.L. Zhou, H.H. Ngo, W. Guo, M.A.H. Johir, K. Sornalingam, Single and competitive sorption properties and mechanism of functionalized biochar for removing sulfonamide antibiotics from water, Chem. Eng. J., 311 (2017) 348–358.

[11] J.D. Dai, A. Xie, R.L. Zhang, W.N. Ge, Z.S. Chang, S.J. Tian, C.X. Li, Y.S. Yan, Scalable preparation of hierarchical porous carbon from lignin for highly efficient adsorptive removal of sulfamethazine antibiotic, J. Mol. Liq., 256 (2018) 203–212.

[12] S.X. Chen, J. Wang, Z.L. Wu, Q. Deng, W.F. Tu, G.P. Dai, Z.L. Zeng, S.G. Deng, Enhanced Cr(VI) removal by polyethylenimine- and phosphorus-codoped hierarchical porous carbons, J. Colloid Interface Sci., 523 (2018) 110–120.

[13] L. Nielsen, T.J. Bandosz, Analysis of sulfamethoxazole and trimethoprim adsorption on sewage sludge and fish waste derived adsorbents, Microporous Mesoporous Mater., 220 (2016) 58–72.

[14] I. Ahmed, B.N. Bhadra, H.J. Lee, S.H. Jhung, Metal-organic framework-derived carbons: preparation from ZIF-8 and application in the adsorptive removal of sulfamethoxazole from water, Catal. Today, 301 (2018) 90–97.

[15] X. Li, H. Yuan, X. Quan, S. Chen, S.J. You, Effective adsorption of sulfamethoxazole, bisphenol A and methyl orange on nanoporous carbon derived from metal-organic frameworks, J. Environ. Sci., 63 (2017) 250–259.

[16] W. Zheng, Y.W. Shi, G.Z. Liu, B. Zhao, L. Wang, Heteroatom-doped highly porous carbons prepared by *in situ* activation for efficient adsorptive removal of sulfamethoxazole, RSC Adv., 10 (2020) 1595–1602.

[17] Y.K. Lan, T.C. Chen, H.J. Tsai, H.C. Wu, J.H. Lin, I.K. Lin, J.F. Lee, C.S. Chen, Adsorption behavior and mechanism of antibiotic sulfamethoxazole on carboxylic-functionalized carbon nanofibers-encapsulated Ni magnetic nanoparticles, Langmuir, 32 (2016) 9530–9539.

[18] A.-H. Lu, E.L. Salabas, F. Schüth, Magnetic nanoparticles: synthesis, protection, functionalization, and application, Angew. Chem. Int. Ed., 46 (2007) 1222–1244.

[19] J.L. Wan, H.P. Deng, J. Shi, L. Zhou, T. Su, Synthesized magnetic manganese ferrite nanoparticles on activated carbon for

[20] F. Wang, W.L. Sun, W.Y. Pan, N. Xu, Adsorption of sulfamethoxazole and 17β-estradiol by carbon nanotubes/CoFe$_2$O$_4$ composites, Chem. Eng. J., 274 (2015) 17–29.

[21] F. Reguyal, A.K. Sarmah, W. Gao, Synthesis of magnetic biochar from pine sawdust via oxidative hydrolysis of FeCl$_2$ for the removal sulfamethoxazole from aqueous solution, J. Hazard. Mater., 321 (2017) 868–878.

[22] J.Y. Heo, Y.M. Yoon, G.Y. Lee, Y.J. Kim, J.H. Han, C.M. Park, Enhanced adsorption of bisphenol A and sulfamethoxazole by a novel magnetic CuZnFe$_2$O$_4$–biochar composite, Bioresour. Technol., 281 (2019) 179–187.

[23] C. Liu, Y.P. Wang, Y.T. Zhang, R.Y. Li, W.D. Meng, Z.L. Song, F. Qi, B.B. Xu, W. Chu, D.H. Yuan, B. Yu, Enhancement of Fe@ porous carbon to be an efficient mediator for peroxymonosulfate activation for oxidation of organic contaminants: incorporation NH$_2$-group into structure of its MOF precursor, Chem. Eng. J., 354 (2018) 835–848.

[24] M. Angamuthu, G. Satishkumar, M.V. Landau, Precisely controlled encapsulation of Fe$_3$O$_4$ nanoparticles in mesoporous carbon nanodisk using iron based MOF precursor for effective dye removal, Microporous Mesoporous Mater., 251 (2017) 58–68.

[25] Y. Yusran, D. Xu, Q.R. Fang, D.L. Zhang, S.L. Qiu, MOF-derived Co@N-C nanocatalyst for catalytic reduction of 4-nitrophenol to 4-aminophenol, Microporous Mesoporous Mater., 241 (2017) 346–354.

[26] J.J. Zhang, X.L. Yan, X.Y. Hu, R. Feng, M. Zhou, Direct carbonization of Zn/Co zeolitic imidazolate frameworks for efficient adsorption of Rhodamine B, Chem. Eng. J., 347 (2018) 640–647.

[27] M. Sevilla, C. Salinas Martínez-de Lecea, T. Valdés-Solís, E. Morallón, A.B. Fuertes, Solid-phase synthesis of graphitic carbon nanostructures from iron and cobalt gluconates and their utilization as electrocatalyst supports, Phys. Chem. Chem. Phys., 10 (2008) 1433–1442.

[28] J. Xiong, M.H. Hu, X.P. Li, H.Y. Li, X. Li, X. Liu, G.Z. Cao, W.S. Li, Porous graphite: a facile synthesis from ferrous gluconate and excellent performance as anode electrocatalyst of microbial fuel cell, Biosens. Bioelectron., 109 (2018) 116–122.

[29] M. Sevilla, A.B. Fuertes, A general and facile synthesis strategy towards highly porous carbons: carbonization of organic salts, J. Mater. Chem. A, 1 (2013) 13738.

[30] J.D. Dai, S.J. Tian, Y.H. Jiang, Z.S. Chang, A. Xie, R.L. Zhang, Y.S. Yan, Facile synthesis of porous carbon sheets from potassium acetate *via in-situ* template and self-activation for highly efficient chloramphenicol removal, J. Alloys Compd., 732 (2018) 222–232.

[31] B. Xu, D.F. Zheng, M.Q. Jia, G.P. Cao, Y.S. Yang, Nitrogen-doped porous carbon simply prepared by pyrolyzing a nitrogen-containing organic salt for supercapacitors, Electrochim. Acta, 98 (2013) 176–182.

[32] Z.-H. Zhang, Z. Han, X.-A. Zeng, M.-S. Wang, The preparation of Fe-glycine complexes by a novel method (pulsed electric fields), Food Chem., 219 (2017) 468–476.

[33] Y.W. Shi, J.D. Zhu, G. Yuan, G.Z. Liu, Q.F. Wang, W.J. Sun, B. Zhao, L. Wang, H.W. Zhang, Activation of persulfate by EDTA-2K-derived nitrogen-doped porous carbons for organic contaminant removal: radical and non-radical pathways, Chem. Eng. J., 386 (2020) 124009.

[34] N. Ninwiwek, P. Hongsawat, P. Punyapalakul, P. Prarat, Removal of the antibiotic sulfamethoxazole from environmental water by mesoporous silica-magnetic graphene oxide nanocomposite technology: adsorption characteristics, coadsorption and uptake mechanism, Colloids Surf., A, 580 (2019) 123716.

[35] T. Van Tran, D.T.C. Nguyen, H.-T. Nguyen, S. Nanda, D.-V.N. Vo, S.T. Do, T. Van Nguyen, T.A.D. Thi, L.G. Bach, T.D. Nguyen, Application of Fe-based metal-organic framework and its pyrolysis products for sulfonamide treatment, Environ. Sci. Pollut. Res. Int., 26 (2019) 28106–28126.

[36] T.A. Saleh, Naeemullah, M. Tuzen, A. Sarı, Polyethylenimine modified activated carbon as novel magnetic adsorbent for the

removal of uranium from aqueous solution, Chem. Eng. Res. Des., 117 (2017) 218–227.

[37] P. Singjai, T. Thongtem, S. Kumfu, S. Thongtem, Synthesis of CNTs via ethanol decomposition over ball-milled $Fe_2O_3$ coated copper sheets, Inorg. Mater., 43 (2007) 143–147.

[38] P.L. Tan, Active phase, catalytic activity, and induction period of Fe/zeolite material in nonoxidative aromatization of methane, J. Catal., 338 (2016) 21–29.

[39] C. Liu, L.Y. Liu, X. Tian, Y.P. Wang, R.Y. Li, Y.T. Zhang, Z.L. Song, B.B. Xu, W. Chu, F. Qi, A. Ikhlaq, Coupling metal–organic frameworks and $g-C_3N_4$ to derive Fe@N-doped graphene-like carbon for peroxymonosulfate activation: upgrading framework stability and performance, Appl. Catal., B, 255 (2019) 117763.

[40] Z. Cao, X. Liu, J. Xu, J. Zhang, Y. Yang, J.L. Zhou, X.H. Xu, G.V. Lowry, Removal of antibiotic florfenicol by sulfide-modified nanoscale zero-valent iron, Environ. Sci. Technol., 51 (2017) 11269–11277.

[41] X.J. Hou, X.P. Huang, Z.H. Ai, J.C. Zhao, L.Z. Zhang, Ascorbic acid/Fe@$Fe_2O_3$: a highly efficient combined Fenton reagent to remove organic contaminants, J. Hazard. Mater., 310 (2016) 170–178.

[42] J. Pallarés, A. González-Cencerrado, I. Arauzo, Production and characterization of activated carbon from barley straw by physical activation with carbon dioxide and steam, Biomass Bioenergy, 115 (2018) 64–73.

[43] Y.W. Shi, G.Z. Liu, L. Wang, X.W. Zhang, Efficient adsorptive removal of dibenzothiophene from model fuel over heteroatom-doped porous carbons by carbonization of an organic salt, Chem. Eng. J., 259 (2015) 771–778.

[44] Y.W. Shi, G.Z. Liu, L. Wang, H.W. Zhang, Activated carbons derived from hydrothermal impregnation of sucrose with phosphoric acid: remarkable adsorbents for sulfamethoxazole removal, RSC Adv., 9 (2019) 17841–17851.

[45] Y.W. Shi, G.Z. Liu, L. Wang, H.W. Zhang, Heteroatom-doped porous carbons from sucrose and phytic acid for adsorptive desulfurization and sulfamethoxazole removal: a comparison between aqueous and non-aqueous adsorption, J. Colloid Interface Sci., 557 (2019) 336–348.

[46] M. Kah, G. Sigmund, F. Xiao, T. Hofmann, Sorption of ionizable and ionic organic compounds to biochar, activated carbon and other carbonaceous materials, Water Res., 124 (2017) 673–692.

[47] D.Q. Zhu, J.J. Pignatello, Characterization of aromatic compound sorptive interactions with black carbon (charcoal) assisted by graphite as a model, Environ. Sci. Technol., 39 (2005) 2033–2041.

[48] M. Keiluweit, M. Kleber, Molecular-level interactions in soils and sediments: the role of aromatic $\pi$-systems, Environ. Sci. Technol., 43 (2009) 3421–3429.

[49] H.N. Tran, S.-J. You, A. Hosseini-Bandegharaei, H.-P. Chao, Mistakes and inconsistencies regarding adsorption of contaminants from aqueous solutions: a critical review, Water Res., 120 (2017) 88–116.

[50] K.L. Tan, B.H. Hameed, Insight into the adsorption kinetics models for the removal of contaminants from aqueous solutions, J. Taiwan Inst. Chem. Eng., 74 (2017) 25–48.

[51] N.F. Nejad, E. Shams, M.K. Amini, J.C. Bennett, Ordered mesoporous carbon CMK-5 as a potential sorbent for fuel desulfurization: application to the removal of dibenzothiophene and comparison with CMK-3, Microporous Mesoporous Mater., 168 (2013) 239–246.

[52] X. Wei, Z.D. Zhang, L. Qin, J.D. Dai, Template-free preparation of yeast-derived three-dimensional hierarchical porous carbon for highly efficient sulfamethazine adsorption from water, J. Taiwan Inst. Chem. Eng., 95 (2019) 532–540.

[53] Z.A. Jamiu, T.A. Saleh, S.A. Ali, Synthesis of a unique cross-linked polyzwitterion/anion with an aspartic acid residue and its use for $Pb^{2+}$ removal from aqueous solution, RSC Adv., 5 (2015) 42222–42232.

[54] W. Chen, Z.-Y. Ouyang, C. Qian, H.-Q. Yu, Induced structural changes of humic acid by exposure of polystyrene microplastics: a spectroscopic insight, Environ. Pollut., 233 (2018) 1–7.